Analysis of phase sensitivity for binary computer-generated holograms

Yu-Chun Chang, Ping Zhou, and James H. Burge

A binary diffraction model is introduced to study the sensitivity of the wavefront phase of binary computer-generated holograms on groove depth and duty-cycle variations. Analytical solutions to diffraction efficiency, diffracted wavefront phase functions, and wavefront sensitivity functions are derived. The derivation of these relationships is obtained by using the Fourier method. Results from experimental data confirm the analysis. Several phase anomalies were discovered, and a simple graphical model of the complex fields is applied to explain these phenomena. © 2006 Optical Society of America

OCIS codes: 050.1380, 090.2880, 120.2880.

1. Introduction

Computer-generated holograms (CGHs) are diffractive optical elements synthesized with the aid of computers. CGHs use diffraction to create wavefronts of light with desired amplitudes and phases. As a null corrector, CGH is widely used in aspheric surface testing.[1,2] A common type of CGH is a binary hologram, which consists of patterns of curved lines drawn onto or etched into glass substrates. The patterns in a binary CGH may be interpreted as bright and dark interference fringes. A binary CGH can store both the amplitude and phase information of the complex wavefronts by controlling positions, widths, and groove depths of the recorded patterns. The design of a CGH is separated into two parts that allow the independent determination of amplitude and phase of the diffracted light. The structure of the lines, such as the groove depth, or duty cycle, is set to give the appropriate diffraction efficiency. The overall pattern of lines is chosen to give the correct shape of the wavefront. For precise measurement, the error influence must be well known and characterized. The CGH pattern errors and surface figure errors of the substrate have been specified and separated by the absolute testing method.[3,4] Nevertheless, the sensitivity of phase to the duty cycle

and groove depth, which is also very important for optical testing, is less known.

We investigate the effects of duty-cycle and phase depth variations of CGHs on the diffracted wavefront phase. A binary diffraction model, which is assumed to be in the scalar regime, is used for analysis. Diffraction of the wavefront phase is expressed mathematically as a function of the duty cycle and phase depth. Analytical solutions of wavefront phase sensitivity to duty-cycle and phase depth deviations are derived. The data from the experiments confirm the analysis results of the model. Also, a graphical representation of diffraction fields is introduced, which provides an intuitive method of diffraction wavefront analysis. Both amplitude and phase values of the diffracted wavefront can be easily obtained from this graphical representation.

2. Diffraction Model

The simplest form of a hologram is a linear diffraction grating, where the spatial frequency of the grating pattern is constant over the entire hologram. A CGH with variable fringe spacing may be viewed as a collection of linear gratings with variable spatial frequencies. By controlling the spatial frequencies of these linear gratings across the CGH, the incident light can be deflected into any desired form. The performance of a CGH may therefore be directly related to the diffraction characteristics of a linear grating.[5] Linear gratings are often used for studies on CGH properties in order to avoid mathematical difficulties in modeling complicated holograms. They are also chosen as the model for our work.

The linear grating model used in this study is assumed to have binary amplitude and phase distributions. A binary linear grating has a surface relief

Yu-Chun Chang is with KLA-Tencor Corporation, One Technology Drive, Milpitas, California 95035. Ping Zhou (pzhou@optics.arizona.edu) and J. H. Burge are with the College of Optical Sciences, University of Arizona, Tucson, Arizona 85721.
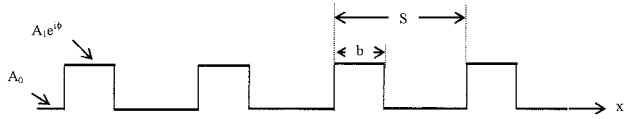
Fig. 1. Output complex wavefront immediately after the diffraction grating.

profile that may be described as an infinite train of rectangular pulses with a uniform width. The wavelength of the incident light is assumed to be much smaller than the grating period (S), so the scalar diffraction approximations can be applied.[6] For a planar wavefront at normal incidence, the output wavefront immediately past the grating, either reflected or transmitted, can be expressed as a simple product of the incident wavefront function and the grating surface profile function. The complex amplitude of the

of a normally incident planar wavefront upon the grating described in Eq. (1) is

$$
\begin{aligned}
U(\xi) &= \Im\{\mathbf{u}(x)\} \\
&= A_0\delta(\xi) + [A_1 \exp(i\phi) \\
&\quad - A_0]b \; \text{sinc}(b\xi) \; \text{comb}(S\xi) \\
&= \left\{ A_0\delta(\xi) + [A_1 \cos(\phi) \right. \\
&\quad \left. - A_0]D \; \text{sinc}(DS\xi) \sum_{m=-\infty}^{\infty} \delta\left(\xi - \frac{m}{S}\right) \right\} \\
&\quad + i\left\{ A_1 \sin(\phi)D \; \text{sinc}(DS\xi) \sum_{m=-\infty}^{\infty} \delta\left(\xi - \frac{m}{S}\right) \right\};
\end{aligned}
$$
(2)

looking at one order at a time,

$$
= \begin{cases} \{A_0 + [A_1 \cos(\phi) - A_0]D\} + i\{A_1 \sin(\phi)D\}, & m = 0 \\ \{[A_1 \cos(\phi) - A_0]D \; \text{sinc}(mD)\} + i\{A_1 \sin(\phi)D \; \text{sinc}(mD)\}, & m = \pm 1, \; \pm 2, \ldots \text{,'} \end{cases}
$$

field, immediately after the grating, can be written as

$$
u(x) = A_0 + [A_1 \exp(i\phi) - A_0]\text{rect}\left(\frac{x}{b}\right)\frac{1}{S} \; \text{comb}\left(\frac{x}{S}\right), \quad (1)
$$

where A_0 and A_1 correspond to the amplitudes of the output wavefronts from the peaks and valleys of the grating, respectively. The values of A_0 and A_1 are determined by the amplitude functions of the reflectance or the transmittance coefficients at the grating interface, using Fresnel equations.[7] The phase function ϕ represents the phase difference between light from the peaks and that from the valleys of the grating. The form of the output wavefront function, shown in Fig. 1, resembles the shape of the grating profile.

Based on Fraunhofer diffraction theory, the far-field diffraction wavefront may be related to the original wavefront by a simple Fourier transform relationship. Hence the far-field wavefront function
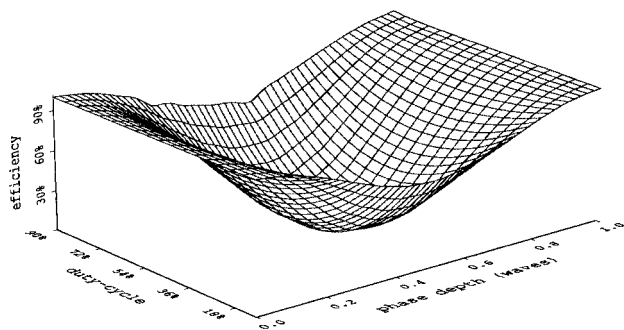
where ξ gives the component of the diffracted light in the direction of $\xi = m\lambda/S$; the duty-cycle D of the linear grating is defined as $D = b/S$; and m is the diffraction order. Equation (2) shows that the diffraction wavefront function $U(\xi)$ has nonzero values only when ξ has a value that is an integer multiple of $1/S$. This behavior describes the existence of multiple diffractive orders. This equation also serves as a foundation for the rest of this study.

A. Diffraction Efficiency

The diffraction efficiency of a specific diffraction order describes the efficiency of the hologram in deflecting light into a particular direction. Diffraction efficiency η is defined as the ratio of the intensity of the dif-

Fig. 2. Diffraction efficiency of a phase grating as a function of the duty cycle and phase depth for the zero-order diffraction beam.
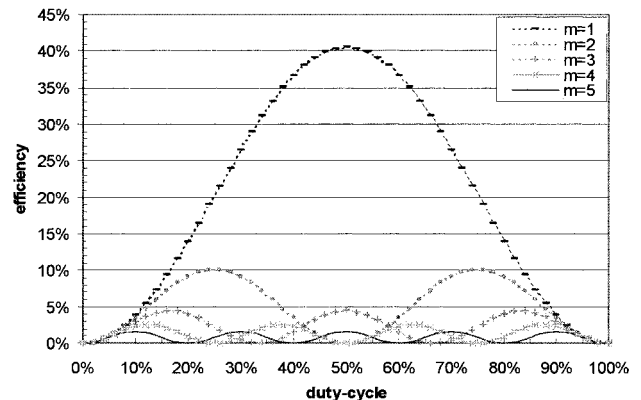

Fig. 3. Diffraction efficiency of phase grating as a function of the duty cycle for the non-zero-order diffraction beams with 0.5λ phase depth.
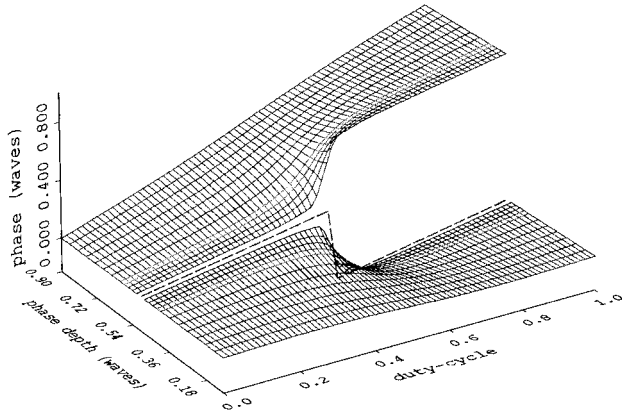
Fig. 4. Diffraction wavefront phase of phase grating as a function of the phase depth and duty cycle for the zero-order diffraction beam.

fracted wavefront to that of the incident wavefront:

$$\eta = \frac{|U(\xi)|^2}{|U_0(\xi)|^2}. \tag{3}$$

Assume the intensity of the incident wavefront $|U_0(\xi)|^2$ is unit. Then, for the zero diffraction order $(m = 0)$,

$$\eta|_{m=0} = A_0^{\,2}(1 - D)^2 + A_1^{\,2}D^2 + 2A_0A_1D(1 - D)\cos(\phi). \tag{4}$$

For nonzero diffraction orders $(m \neq 0)$,

$$\eta|_{m \neq 0} = \left[A_0^{\,2} + A_1^{\,2} - 2A_0A_1\cos(\phi)\right]D^2\,\mathrm{sinc}^2(mD). \tag{5}$$

B. Wavefront Phase

The diffracted wavefront phase function may also be achieved from Eq. (2). The phase function Ψ is defined as the ratio of the imaginary part to the real part of the complex wavefront $U(\xi)$:

$$\tan(\Psi) = \frac{\mathrm{Im}\{U(\xi)\}}{\mathrm{Re}\{U(\xi)\}}. \tag{6}$$

For any single order of diffraction, the phase Ψ can be interpreted as the phase of the plane wave at the grating.

Substituting Eq. (2) into Eq. (6) leads to

$$m = 0: \quad \tan(\Psi)_{m=0}$$
$$= \frac{DA_1 \sin(\phi)}{A_0(1 - D) + A_1D \cos(\phi)}, \tag{7}$$

$$m = \pm1,\ \pm2,\ \ldots: \quad \tan(\Psi)_{m \neq 0}$$
$$= \frac{A_1 \sin(\phi)\mathrm{sinc}(mD)}{[-A_0 + A_1 \cos(\phi)]\mathrm{sinc}(mD)}. \tag{8}$$

The phase can be obtained by taking the arctangent of these equations, and the unit of Ψ is radians. The wavefront phase W in waves can be obtained by

$$W = \frac{\Psi}{2\pi}. \tag{9}$$

Notice that the $\mathrm{sinc}(mD)$ functions are left in both the numerator and denominator of Eq. (8). They need to preserve the sign information for the phase unwrapping process. The phase unwrapping process uses the sign information of the real and imaginary parts of the complex wavefront $U(\xi)$, which allows calculation of phase from the 0 to 2π period. The new phase values are then evaluated point by point. Any integer multiple of 2π can be added or subtracted from the phase value to make the phase function continuous.
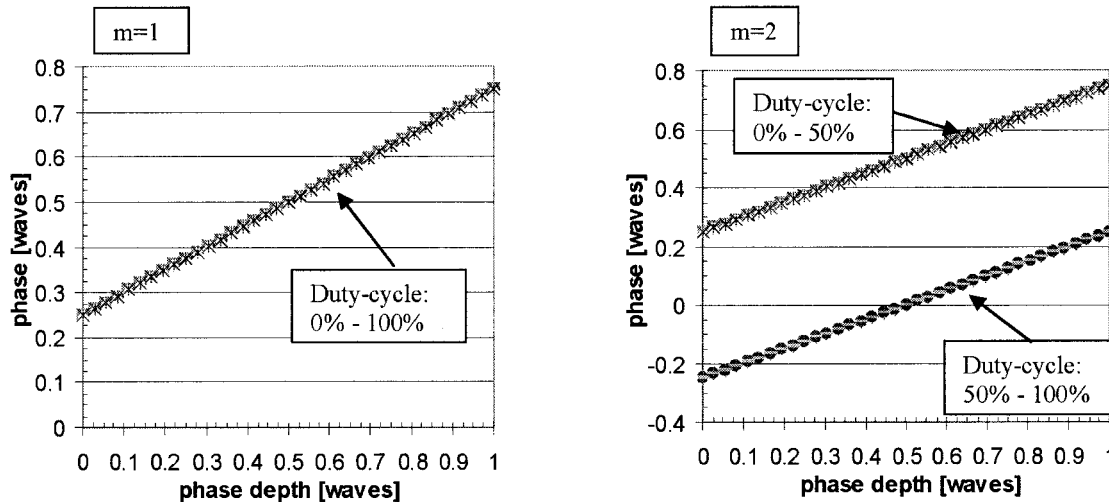

Fig. 5. Wavefront phases versus phase depth for first- and second-order diffraction beams for the phase grating.
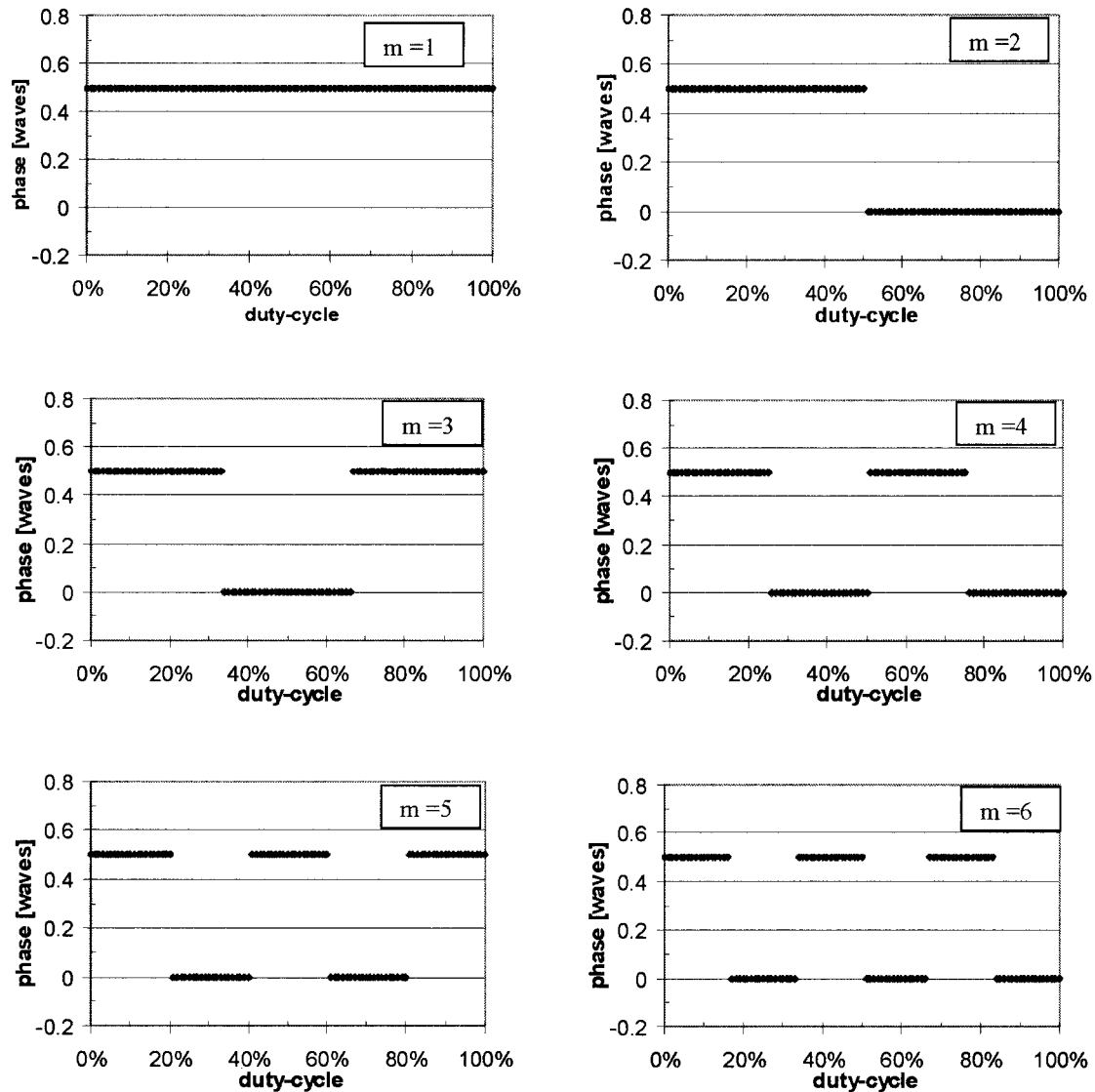
Fig. 6. Wavefront phase versus duty cycle for nonzero diffraction orders at 0.5λ phase depth from phase grating.
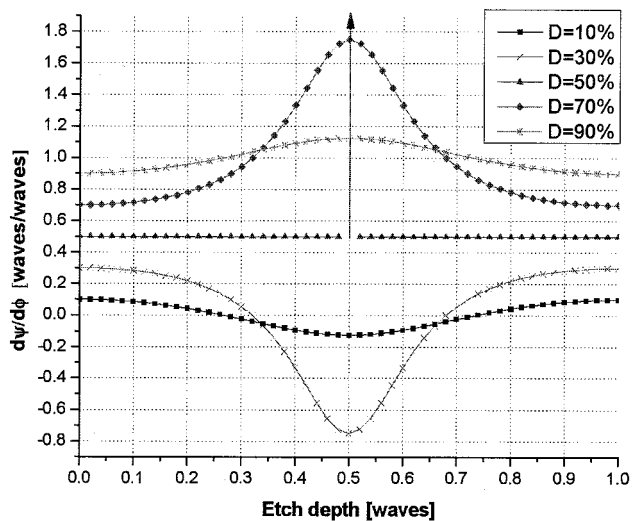

Fig. 7. Analytical result for the wavefront phase sensitivity of phase grating to phase depth variation for the zero-order beam.
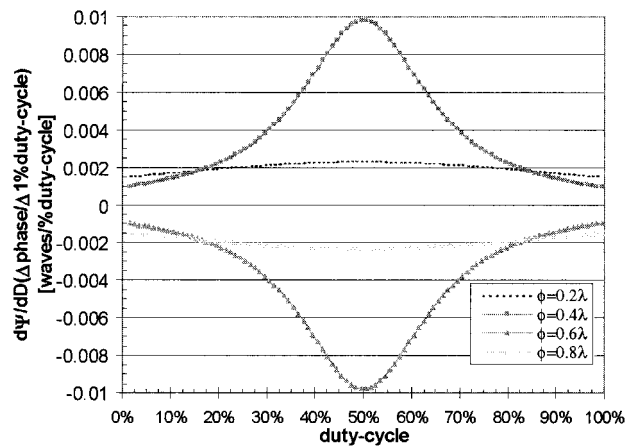

Fig. 8. Analytical result for the wavefront phase sensitivity of phase grating to the duty cycle for the zero-order beam.
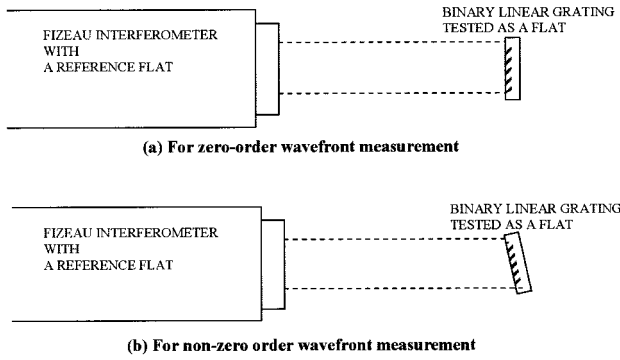
(a) For zero-order wavefront measurement

(b) For non-zero order wavefront measurement

Fig. 9. Experimental setup for diffraction wavefronts measurements of phase grating.

C. Phase Sensitivity to the Duty Cycle

We have shown that the diffracted wavefront phase can be expressed as a function of the duty cycle and phase depth. By taking the first derivative of Eq. (7) and Eq. (8) with respect to either the duty cycle or phase depth, the phase deviations due to the variations of these two parameters can be determined. These deviations are defined as the wavefront sensitivity functions. Equations (10) and (11) show the wavefront sensitivity functions with respect to the grating duty cycle:

$$
\begin{aligned}
m = 0: \quad & \frac{\partial \Psi_{m=0}}{\partial D} \\
= & \frac{1}{1 + [\tan(\Psi)_{m=0}]^2} \frac{\partial \tan(\Psi)_{m=0}}{\partial D} \\
= & \frac{A_0 A_1 \sin \phi}{A_1^2 D^2 + A_0^2 (1-D)^2 + 2A_0 A_1 D(1-D)\cos \phi},
\end{aligned}
\tag{10}
$$

$$
\begin{aligned}
m = \pm 1, \ \pm 2, \ \ldots : \quad & \frac{\partial \Psi_{m \neq 0}}{\partial D} \\
= & \frac{1}{1 + [\tan(\Psi)_{m \neq 0}]^2} \frac{\partial \tan(\Psi)_{m \neq 0}}{\partial D} \\
= & \begin{cases} \infty, & \text{for } \mathrm{sinc}(mD) = 0, \\ 0, & \text{otherwise.} \end{cases}
\end{aligned}
\tag{11}
$$

Notice that duty-cycle errors produce wavefront phase errors only in the zero-order diffraction. The diffraction wavefront phase is not sensitive to CGH duty-cycle errors at nonzero diffraction orders. For the nonzero orders, diffraction efficiency is zero when $\mathrm{sinc}(mD)$ equals to zero, and the sensitivities to the duty cycle go to infinity at those points. Otherwise, in Eq. (8), $\mathrm{sinc}(mD)$ in both numerator and denominator can be cancelled, and the wavefront phase is not sensitive to the duty cycle.

D. Phase Sensitivity to Phase Depth

Similarly, wavefront phase sensitivities to phase depth at different diffraction orders are given as

$$
\begin{aligned}
m = 0: \quad & \frac{\partial \Psi_{m=0}}{\partial \phi} \\
= & \frac{1}{1 + [\tan(\Psi)_{m=0}]^2} \frac{\partial \tan(\Psi)_{m=0}}{\partial \phi} \\
= & \frac{A_1^2 D^2 + A_0 A_1 D(1-D)\cos \phi}{A_1^2 D^2 + A_0^2 (1-D)^2 + 2A_0 A_1 D(1-D)\cos \phi},
\end{aligned}
\tag{12}
$$

$$
\begin{aligned}
m = \pm 1, \ \pm 2, \ \ldots : \quad & \frac{\partial \Psi_{m \neq 0}}{\partial \phi} \\
= & \frac{1}{1 + [\tan(\Psi)_{m \neq 0}]^2} \frac{\partial \tan(\Psi)_{m \neq 0}}{\partial \phi} \\
= & \frac{A_1^2 - A_0 A_1 \cos \phi}{A_1^2 + A_0^2 - 2A_0 A_1 \cos \phi}.
\end{aligned}
\tag{13}
$$

The wavefront sensitivity functions [Eqs. (10)–(13)] provide a means of calculating the phase changes in the wavefront that result from duty-cycle or phase depth variations. They can be used to identify hologram structures that are the most or the least sensitive to duty-cycle and groove depth fabrication uncertainties. The information may also be used to estimate error budgets for the applications of CGHs.[8]

The sensitivity functions can be evaluated directly to give the wavefront error due to variations in the duty cycle or phase depth:

$$
\Delta W_D = \frac{1}{2\pi} \frac{\partial \Psi}{\partial D} \Delta D = \frac{1}{2\pi} \frac{\partial \Psi}{\partial D} \left(\frac{\Delta D}{D} \right) D,
\tag{14}
$$

$$
\Delta W_\phi = \frac{\partial \Psi}{\partial \phi} \Delta \phi = \frac{\partial \Psi}{\partial \phi} \left(\frac{\Delta \phi}{\phi} \right) \phi,
\tag{15}
$$

where ΔD is the duty-cycle variation across the grating; ΔW_D is the phase variation in waves due to duty-cycle variation, $\Delta \phi$ is the phase depth variation in radians across the grating, and ΔW_ϕ is the phase variation in waves due to phase depth variation.

As long as the duty-cycle and phase depth variations vary over spatial scales that are large compared to the grating spacing, we can use the functions above to determine the coupling between fabrication errors and system performance.

3. Numerical Simulations

A linear phase grating with an index of refraction of 1.5 is analyzed with the diffraction model derived in the Section 2. Phase gratings are typically made by etching the grating patterns onto a bare glass substrate, and modulate only the phase function of the incident wavefront. For this analysis, the grating is used in reflection, so the groove depth is half of the phase depth ϕ. If the grating works in transmission, then the groove depth is equal to the phase depth ϕ. An ideal reflection is assumed in our study, so $A_0 = A_1 = 1$.
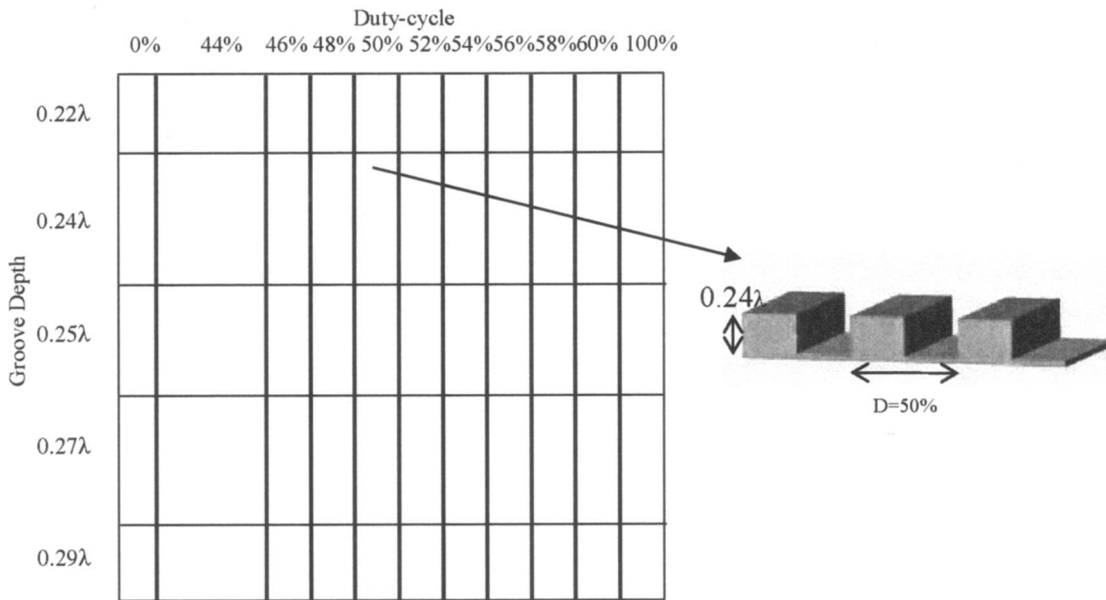
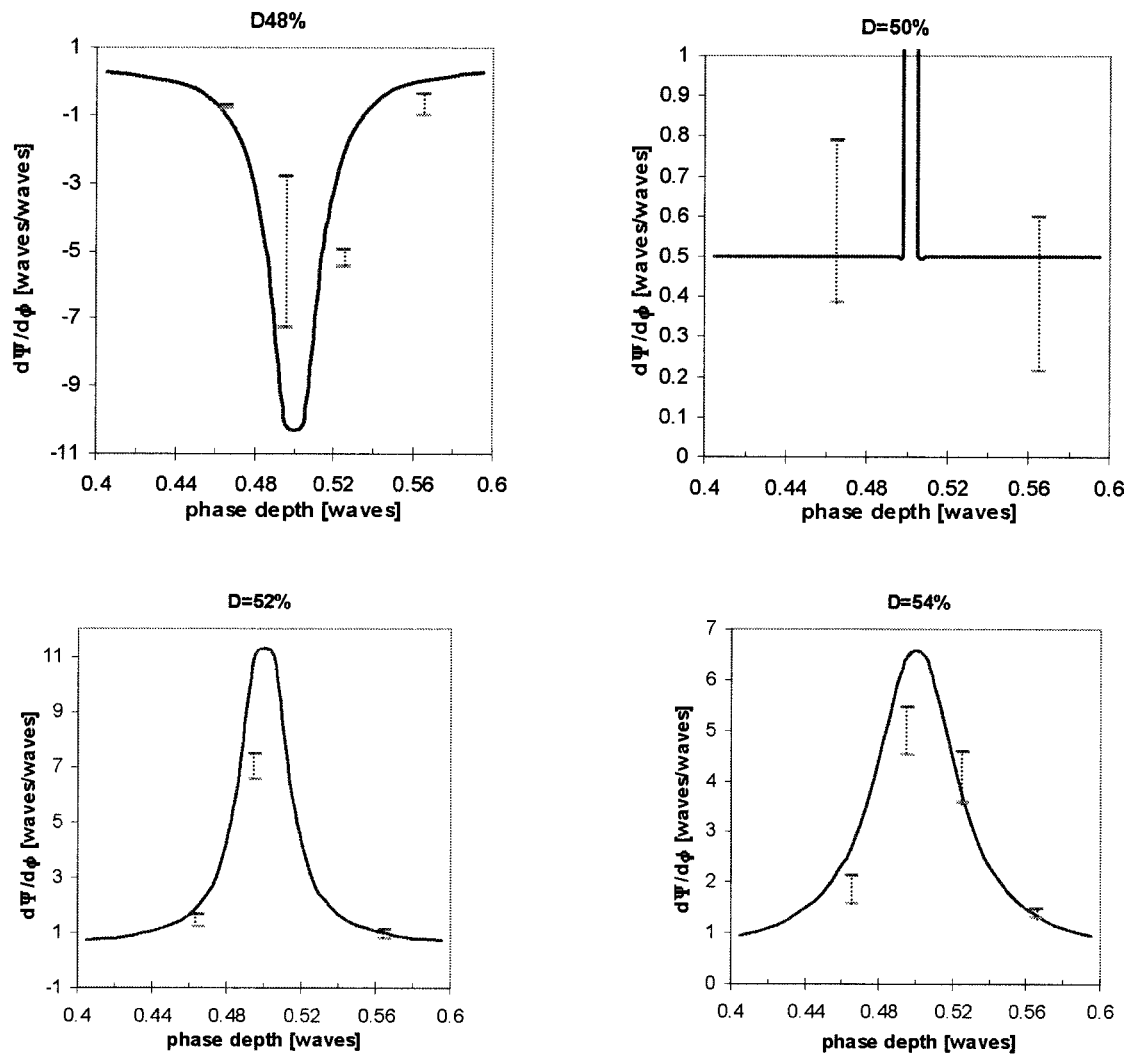Fig. 10.   Design layout of the sample phase grating.

Fig. 11.   Diffraction wavefront phase sensitivities to phase depth for the zero-order beam. Experimental data (vertical bar) versus theoretical results (solid line).
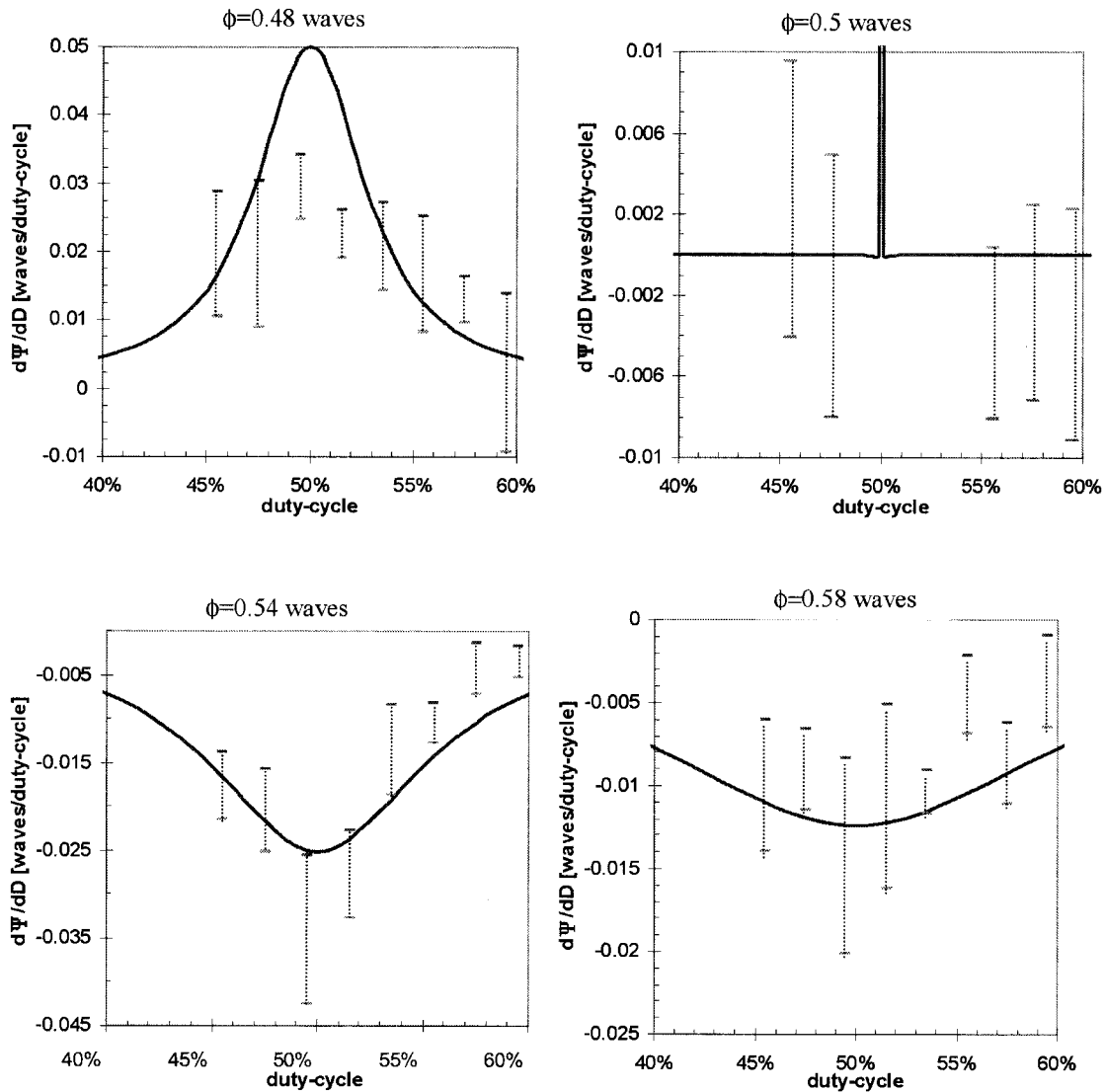
Fig. 12. Diffraction wavefront phase deviations per 1% duty-cycle variation for the zero-order beam. Experimental data (vertical bar) versus theoretical results (solid curve).

A. Diffraction Efficiency

Diffraction efficiencies for the phase grating are calculated using Eqs. (4) and (5). Figure 2 shows the diffraction efficiency as a function of both the duty cycle and phase depth for the zero-order beam. The minimum value of diffraction efficiency occurs at the point where the phase depth is $\lambda/2$ and the duty cycle is 50%. The distribution is symmetric about this point.

Diffraction efficiencies for non-zero-order diffraction fields ($m \neq 0$) vary periodically with changes in the grating duty cycle. Figure 3 shows the diffraction efficiencies of different orders with the phase depth of $\lambda/2$. Moreover, the number of times that maximum efficiency values reach for each diffraction beam is equal to the order number of that beam.

B. Wavefront Phase

Wavefront phase distributions are obtained from Eqs. (7) and (8). Figure 4 shows the diffracted wavefront phase as a function of the phase depth and the duty cycle for the zero-order beam. The phase curves at all duty cycles are continuous as a function of phase depth, with the exception of the 50% duty cycle. An anomalous phase discontinuity is observed along the 50% duty-cycle line at the $\lambda/2$ phase depth point. It implies a phase reversal in the diffracted wavefront when the phase depth reaches the $\lambda/2$ point. The discontinuity also indicates a high sensitivity of the wavefront phase function in the zero diffraction order to groove depth fabrication errors for gratings with a 50% duty cycle and $\lambda/2$ phase depth. Further discussions of this discontinuity are given in Section 5, using the graphical complex field representation.

Phase functions for non-zero-order beams ($m \neq 0$) are shown in both Figs. 5 and 6. Figure 5 gives the relationship between the wavefront phase and the phase depth for all non zero orders. It is shown that the wavefront phase varies linearly with the phase
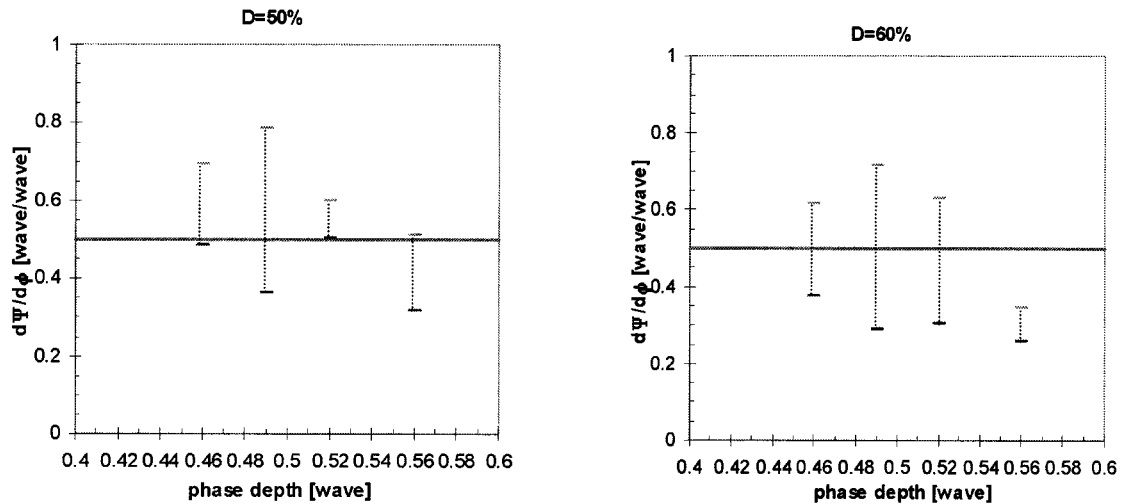
Fig. 13. Wavefront phase sensitivity functions per phase depth variations for the first-order diffraction wavefront. Experimental data (vertical bars) versus theoretical data (solid curve).

depth. It is also obvious that the dependence of wavefront phase on variations in phase depth errors is constant.

Figure 6 shows the relationship between the wavefront phase and duty cycle for non-zero-order beams. Notice that the phase functions exhibit $\lambda/2$ discontinuities for diffraction orders higher than 1. A $\lambda/2$ phase discontinuity occurs at a 50% duty-cycle point for the second-order diffraction beam. Two $\lambda/2$ phase steps occur for the third-order diffraction, at 33.3% and 66.6% duty-cycle points. These phase jumps are the direct results of the sign changes of the $\mathrm{sinc}(mD)$ function in Eq. (8). The alteration between positive and negative values of the sinc function causes the calculated phase values to change by $\pm\pi$ rad. The number of discontinuities that occur when the grating duty cycle varies from 0% to 100% is equal to the diffraction order number minus one. Figure 6 also implies that deviations in the grating duty cycle have

no effect on the wavefront phase for non-zero-order beams.

C. Wavefront Phase Sensitivity

In Subsections 2.C and 2.D, the analytical solutions of diffraction wavefront phase sensitivities to duty-cycle and phase depth variations are derived. Based on these equations, the diffracted wavefront phase sensitivities can be represented in a graphical format.

Figure 7 shows the wavefront phase sensitivity to the phase depth for the zero-order beam. Gratings with various duty cycles are shown. A 0.1λ phase depth error will produce a -0.075λ wavefront phase error for the phase grating with a 30% duty cycle and a nominal phase depth of 0.5λ. The same phase depth error produces a $+0.03\lambda$ wavefront phase error for the phase grating with a 30% duty cycle and a nominal phase depth of 0.1λ. It is also realized that phase
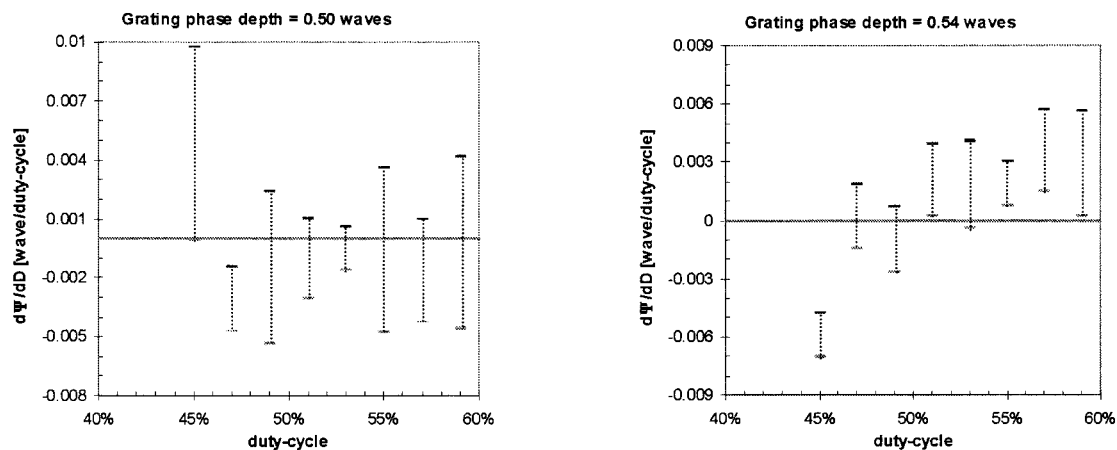

Fig. 14. Wavefront phase sensitivity functions per 1% duty-cycle variations for the first-order diffraction wavefront of phase grating. Experimental data (vertical bars) versus theoretical data (solid curve).
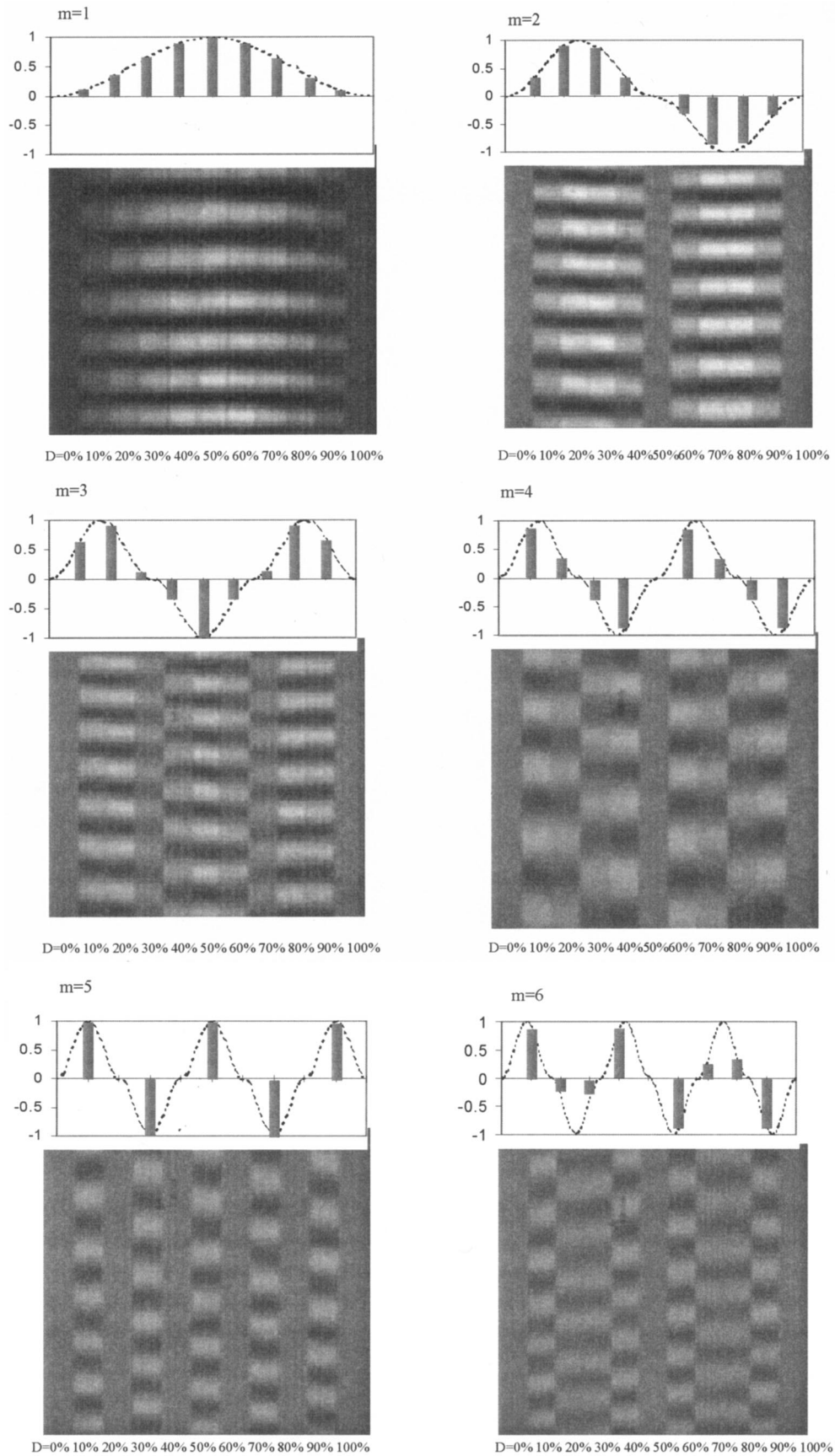
Fig. 15.   Interferogram indicating diffraction efficiency distribution and wavefront phase as a function of the duty cycle at different diffraction orders. The top chart shows the corresponding theoretical values.
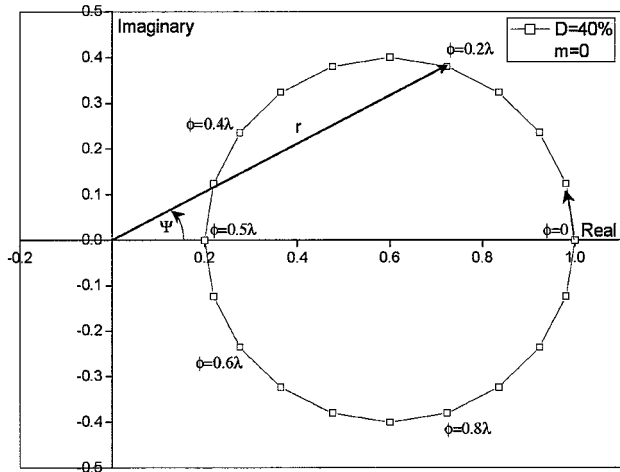
Fig. 16. Graphical representation of the complex diffraction wavefront produced by a phase grating with 40% duty cycle for the zero-order beam.

gratings with a 50% duty cycle are extremely sensitive to the phase depth variations at a 0.5λ nominal phase depth.

Figure 8 illustrates the wavefront phase changes that result from 1% deviations in the duty cycle. For instance, a 1% variation will result in −0.004 waves of phase error in the zero-order beam for phase grating with 30% duty cycle and 0.6 waves nominal phase depth.

Using the wavefront sensitivity functions, wavefront phase and efficiency errors can be estimated with knowledge of the uncertainties from the CGH fabrication processes. The wavefront sensitivity functions can also be used for guidance for the design of CGHs to reduce or eliminate wavefront errors produced by fabrication uncertainties.

4. Validation of Model

To verify the wavefront prediction by the model, two sample phase gratings were fabricated. A phase-shifting Fizeau interferometer was used to measure the diffraction wavefronts produced by the sample gratings, as shown in Fig. 9. The sample grating was treated as a flat test plate, and a transmission flat

with λ/20 accuracy (λ = 632.8 nm) was used as the reference. The distance between the test grating and reference flat was minimized during the experiments in order to reduce air turbulence in the test beam path.

The first sample phase grating was designed for a reference wavelength of 0.633 μm. The sample grating is divided into a 5 × 11 array, where each cell in the array contains a linear grating with the specific duty cycle and phase depth, as shown in Fig. 10. Along the rows of the grating array, the duty cycle varies in 2% increments from 44% to 60%. Duty-cycle gratings of 0% and 100% are placed at the first and the last cell of each row in the grating array. Groove depths or half-phase depths of the columns are 0.22λ, 0.24λ, 0.25λ, 0.27λ, and 0.29λ.

For the zero-order measurement, the sample grating was aligned parallel to the reference surface. Optical interferometric measurements provide information on the wavefront phase of the test beam relative to the reference wavefront. In order to avoid unnecessary complications or confusion when comparing the experimental results with the theoretical data, phase deviations between adjacent grating cells were used in our analysis instead of the absolute phase values. The phase deviation functions in Section 5 represent wavefront phase changes as a result of variations in the grating duty cycle or the phase depth.

Linear gratings with the same duty cycle on the sample grating array were measured together to determine wavefront phase sensitivities as a function of phase depth variations. Measured wavefront phase sensitivities to the phase depth for gratings with various duty cycles are shown in Fig. 11. Theoretical wavefront phase sensitivities are overlaid on the experimental results. The error bars of the experimental data provide information on the noise and confidence level of our results. A large standard deviation of the data implies a high noise level or a large amount of random errors in our measurements. For the phase sensitivities to phase depth analysis, the experimental results agree well with the theoretical data in most cases.

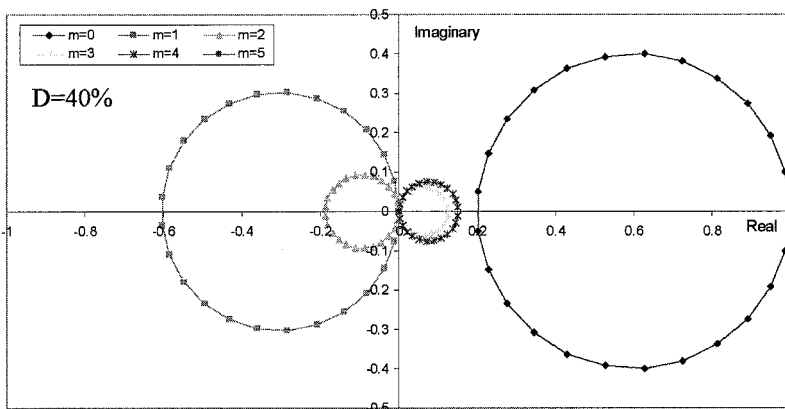Gratings with the same groove depth were mea-

Fig. 17. Graphical representation of the complex diffraction fields at five different diffraction orders for a phase grating with a 40% duty cycle.
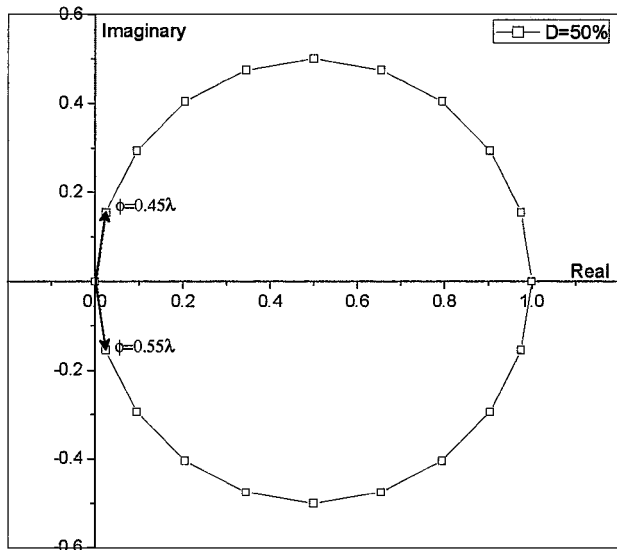
Fig. 18. Graphical representation of the complex diffraction fields in zero diffraction order produced by a phase grating with a 50% duty cycle.

sured together in order to determine wavefront phase sensitivities as a function of grating duty-cycle variations. Wavefront phase deviations per 1% duty-cycle variations for gratings with various phase depths are given in Fig. 12. Although the measured data did not agree perfectly with the theoretical predication, general behaviors hypothesized by our analytical models were clearly observed. And the measured wavefront sensitivities to the duty cycle are within the theoretical scale. Random errors, such as the substrate nonflatness and measurement errors, may result in the deviations of the measured data from the theoretical calculations.

To measure the first diffraction order wavefront, the sample grating was tilted with respect to the reference flat, so that the first-order beam was
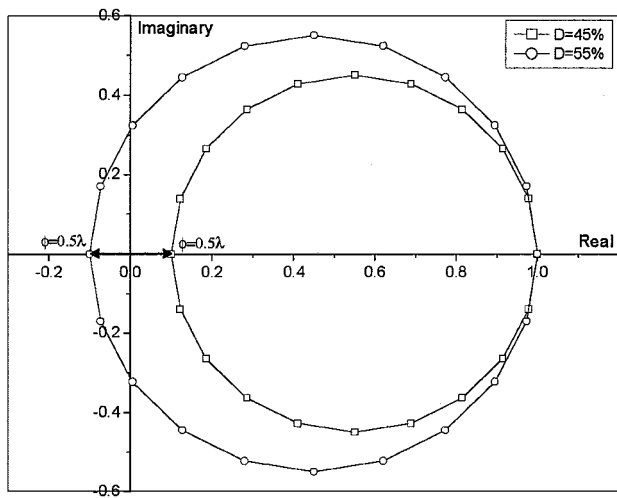

Fig. 19. Graphical representation of the complex diffraction fields in zero diffraction order produced by a phase grating with 45% and 55% duty cycles.

seen by the interferometer [Fig. 9(b)]. Our analytical model predicts constant sensitivity to phase depth variations for all non-zero-order diffraction beams. This agrees with the measured data, shown in Fig. 13.

The measured wavefront sensitivities to grating duty-cycle variations are shown in Fig. 14. According to our analytical model, the diffracted wavefront phases are not sensitive to grating duty-cycle variations. The measured data agree well with this theoretical predication.

The second grating sample was fabricated with duty cycles ranging from 0% to 100%, in 10% increments and with a constant groove depth. As shown in Fig. 3, the diffraction efficiency for nonzero beams varies periodically with changes in the grating duty cycle, and the number of times that maximum efficiencies can be obtained for each diffraction order is equal to the order number. Also recall Fig. 6 shows that phase discontinuity occurs when $\mathrm{sinc}(mD) = 0$. These predictions can be verified directly with the help of interferograms obtained from the sample grating, as shown in Fig. 15. Parallel fringes seen across the vertical direction (y direction) of all interferograms indicate the tilt of the sample grating in the vertical direction. The tilt of the sample grating in the horizontal direction was eliminated. Observed intensity levels along the x direction of the interferograms correspond directly to the diffraction efficiencies of gratings with various duty cycles at each diffraction order. A normalized intensity distribution plot based on the theoretical diffraction efficiency is above each interferogram. The phase reversal effects between different grating duty cycles are also included in the intensity plots. Discontinuities of the fringes in the interferograms correspond to the discontinuities of the phase function, or phase reversal. As seen from Fig. 15, observed intensity distribution functions agree perfectly with the theoretical predictions. Periodicity of the diffraction efficiency functions for the non-zero-order beams produced by the sample gratings can be clearly identified. Phase reversals, or $\lambda/2$ phase discontinuities, are also observed in the interferograms.

5. Graphical Representation of Diffraction Fields

A. Representation of Diffraction in the Complex Plane

Diffraction fields may be represented by plotting the real and the imaginary parts of the diffraction wavefronts in a complex coordinates. This graphical representation provides an intuitive view of the diffracted wavefront phase function. Both diffraction efficiency and wavefront phase values may be easily obtained from the plot. Figure 16 gives a demonstration of this graphical representation. The circle in the plot contains the complete solutions of a phase grating with a 40% duty cycle at the zero-order diffraction. Each point in the circle corresponds to different values of phase depth. A vector (**r**) pointing from the origin of the complex coordinate to a point on the circle corresponds to a solution of the diffraction fields

produced by the grating at a specific phase depth. As the grating phase depth increases, the tip of vector travels along the circle in the counterclockwise direction that is indicated by the arrow in the figure. The magnitude of the vector ($\mathbf{r}$) gives the amplitude of the diffraction field, while the angle between the vector ($\mathbf{r}$) and the real axis gives the phase value (Ψ) of the diffraction field.

As an example, in Fig. 16 the vector $\mathbf{r}$ is pointing to the $\phi = 0.2\lambda$ point on the circle. This point corresponds to the zero-order diffraction beam of a phase grating with a 40% duty cycle and 0.2 waves of phase depth. The magnitude of the vector is 0.82 and the corresponding efficiency is $\eta = 0.82^2 = 67\%$. The angle between the vector $\mathbf{r}$ and the real axis is approximately 28°, which gives a wavefront phase $\Psi = 28°/360° = 0.077$. Figure 17 illustrates the graphical representations of the complex diffraction fields for both zero and nonzero diffraction orders. Those graphical representations can be directly derived from Eq. (2).

B. Graphical Explanation of Phase Anomaly

One advantage of the complex field plot is that anomalous phase discontinuities can be explained easily. Recall Fig. 4 where a phase discontinuity was observed for the zero-order diffraction beam along the 50% duty-cycle line at a $\lambda/2$ phase depth. The explanation of the phase discontinuity was not obvious from the derived equations. However, it may be explained directly using the complex field representation.

Figure 18 gives the graphical representation of the zero-order diffraction field at 50% duty cycle with the phase depth varied from zero to one wave. The zero phase depth point is located on the real axis one unit away from the origin. As the phase depth increases, the solution point travels counterclockwise along the circle. For the phase depth of 0.45λ and 0.55λ, the wavefront phases are 81° and −81°, respectively. The phase change is about 162°. When the vector ($\mathbf{r}$) passes the origin, where the phase depth equals to $\lambda/2$, the angle of the vector varies abruptly from +90° to −90°, or the wavefront displays a π phase change. At this point, the diffraction efficiency of the grating is zero. Therefore, the apparent discontinuity in phase is actually a continuous transition in the complex field.

Figure 19 shows how the wavefront phase changes with respect to the duty cycle at the 0.5λ phase depth. For the duty cycles of 45% and 55%, the wavefront phases are 0° and 180°, respectively. For duty cycles of less than 50%, the wavefront phases at the 0.5λ phase depth are 0°. Likewise, the wavefront phases are 180° for duty cycles greater than 50%. It means there is a discontinuity at the point where the duty cycle is 50%.

6. Conclusion

We have shown that the method of Fourier analysis can be applied to determine wavefront phase as well as amplitude and diffraction efficiency. The validity of this analysis is demonstrated by direct measurement of wavefront phase using an interferometer. We noted two interesting cases where the phase can jump abruptly by a half-wave. These jumps are predicted by the Fourier model and they can be readily explained using a graphical depiction of how the diffracted wavefront behaves in the complex plane.

References

1. S. Reichelt, C. Pruß, and H. J. Tiziani, "New design techniques and calibration methods for CGH-null testing of aspheric surfaces," in Proc. SPIE **4778,** 158–168 (2002).
2. T. Herrmann, "Testing aspheric surfaces with CGH of different accuracy in industrial manufacturing environ," in Proc. SPIE **4440,** 120–126 (2001).
3. C. Pruss, S. Reichelt, H. J. Tiziani, and W. Osten, "Computer-generated holograms in interferometric testing," Opt. Eng. **43,** 2534–3540 (2004).
4. S. Reichelt, C. Pruß, and H. J. Tiziani, "Specification and characterization of CGHs for interferometrical optical testing," in Proc. SPIE **4778,** 206–216 (2002).
5. G. J. Swanson, "Binary optics technology: theoretical limits on the diffraction efficiency of multilevel diffractive optical elements," technical report (Lincoln Library, Massachusetts Institute of Technology, 1991).
6. J. Gaskill, *Linear Systems, Fourier Transforms, and Optics* (Wiley, 1978).
7. M. Born and E. Wolf, *Principles of Optics,* 6th ed. (Cambridge U. Press, 1980).
8. Y. C. Chang and J. H. Burge, "Errors analysis for CGH optical testing," in *Optical Manufacturing and Testing III*, Proc. SPIE **3782,** 358–366 (1999).